Fluid Flow Visualization by Three-dimensionally Reconstructed Tracer Path Lines

Machacek, M.[*1] and Rösgen, T.[*2]

*1   Institute of Fluid Dynamics, ETH Zürich, Sonneggstr. 3, CH-8092 Zürich, Switzerland.
     E-mail: machacek@ifd.mavt.ethz.ch
*2   Institute of Fluid Dynamics, ETH Zürich.

Abstract : The development of a measurement system for the visualization, topological classification and quantitative analysis of complex flows in large-scale wind tunnel experiments is described. A new approach is sought whereby the topological features of the flow, e.g. stream lines, separation and reattachment regions, stagnation points and vortex lines are extracted directly and are preferably visualized in real-time in a virtual wind tunnel environment. The system is based on a stereo arrangement of two CCD cameras. A frame rate of 120 f/s allows measurements at high flow velocities. Helium filled soap bubbles are used as tracer particles. The present paper describes a simple camera calibration procedure for large measurement environments and examines the problem of fast and accurate reconstruction of path lines in three dimensions, which will enable true three-dimensional and time-resolved fluid flow visualization. Experimentally obtained visualization results for a free-stream flow, flow around a circular plate and flow over a delta wing are presented.

Keywords : Three-dimensional flow visualization, Topology, Path lines, Camera calibration, Helium-filled bubbles.

1. Introduction

Classical visualization methods, such as the smoke wire, the laser vapor screen, and tufts, provide an overview of the flow topology, but quantitative data is often not available and much depends on the interpretation by the researcher. The alternative is to combine classical qualitative visualization methods and modern computer vision technology to generate quantitative data. The intuitiveness of the visualization approach is maintained by representing the results in a "virtual wind tunnel" environment with an interactive user interface. The priority in the present approach is not to generate dense spatial measurement data, but rather continuous temporal measurements in a three-dimensional measurement volume. One possible way to obtain such data is to measure continuous particle path lines directly.

The described method is based on helium filled bubbles as flow tracers. The camera and illumination are configured such that images of moving particles represent path lines. This is the

fundamental difference from conventional particle tracking methods, which are based on "frozen" images of particles (Takehara and Etoh 1999; Doh et al. 2002). The spatial processing of the acquired image data is done based on the principles of the photogrammetry theory (Hartley and Zisserman, 2000). A key element of the system is an accurate and simple camera calibration. To facilitate the calibration procedure for large measurement volumes while maintaining a simple and fast procedure, a two-step self-calibration is employed.
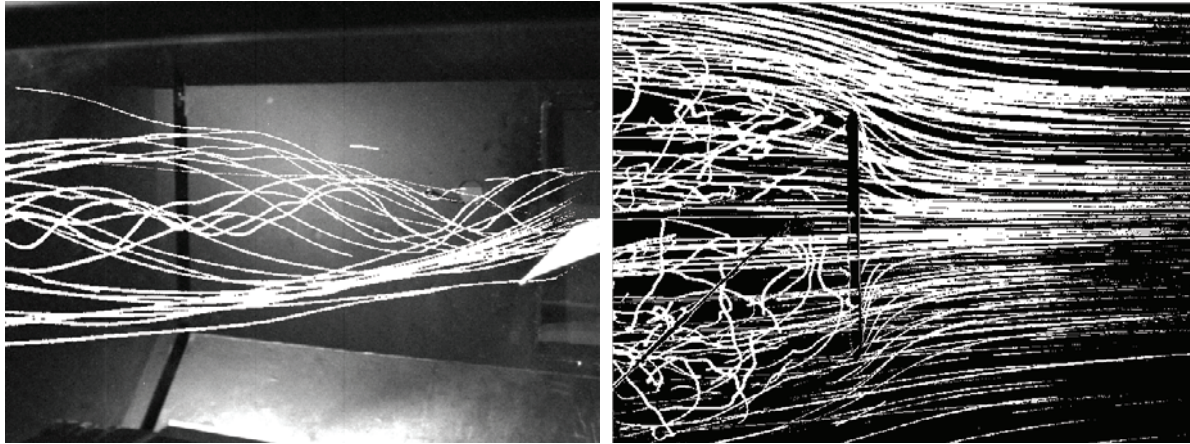

Fig. 1. Path lines created by helium-filled bubbles in a flow around a delta wing (left) and a flow around a circular plate (right). The path lines, which contain a great deal of information on flow velocity and topology, are used herein for quantitative flow visualization.

2. Experimental Setup

The visualization system consists of the following components. Two progressive-scan interline CCD cameras record images at a frame rate of 120 f/s and with a resolution of 640x480 pixels. Lighting is provided by four halogen spot lamps with a total power of 6,000 W. The helium filled soap bubbles for seeding are introduced into the test section through a strut mounted nozzle. The bubbles have an approximate diameter of 2 mm. The components are set up in a wind tunnel with a cross section of 2 x 3 m which is capable of achieving wind speeds of up to 60 m/s.

3. Camera Model

3.1 Camera Model Parameters

The camera model describing the mapping of a "real space" point $\underline{X} \in \boldsymbol{R}^3$ onto a "pixel point" $\underline{x}_p \in \boldsymbol{R}^2$ used in the present study is the pinhole model adopted from photogrammetry theory (Hartley and Zisserman, 2000). The model parameters considered herein are the focal length f, the principal point (x_0, y_0), the stretching of the x-axis s_x and the skew θ, respectively. In addition, lens distortion is compensated for by two polynomials for the radial distortion (k_1, k_2) and for the tangential distortion (p_1, p_2). The camera position and orientation with respect to a global coordinate system is described by the parameters (X_0, Y_0, Z_0) and $(\varphi, \omega, \kappa)$. The pixel width and height (p_w, p_h) are assumed to be known. This represents a camera model with a total of 15 a priori parameters. A

look-up table is constructed for the mapping from pixel space coordinates to normalized[1] image coordinates. This provides significantly faster processing of the nonlinear part of the overall coordinate transform and reduces the subsequent processing to linear operations, despite the nonlinear formulation.

3.2 Camera Calibration

A precise camera calibration is essential to obtain both a reliable matching of features between two camera views and an accurate three-dimensional reconstruction. The calibration procedure should also be easy to perform in order to meet the tight experiment schedules often required in industrial wind tunnel measurements. This becomes crucial for measurements in large volumes, where an accurate calibration requires an adequately large calibration target. Such a large calibration target would likely be difficult to manipulate, and expensive and difficult to produce within the accuracy required for a reliable calibration. Therefore, a two-step calibration strategy is deployed which combines the accuracy of a photogrammetric calibration with the advantages of self-calibration. In the first stage, the inner camera parameters (f, x_0, y_0, s_x, θ, k_1, k_2, p_1, p_2) are calibrated with a photogrammetric method based on a calibration target of known shape and dimension (Machacek and Rösgen, 2000). Since these parameters do not depend on the camera position, this calibration has to be done only once for a given camera/lens configuration and the target can be of arbitrary size. For the calculation of the external parameters (X_0, Y_0, Z_0, φ, ω, κ), a self-calibration method based on the information of point correspondences between the two views and a reference length L is used. This method is based on the *normalized 8-point algorithm* described in detail by Longuet-Higgins (1981) and Hartley and Zisserman (2000) and on the calibration target proposed by Borghese and Cerveri (2000).

The essential matrix $\boldsymbol{E}$ is calculated based on corresponding normalized[2] points obtained from the two camera views. Thereafter, the essential matrix is decomposed into rotational and translational components which leads to the camera rotation matrix $\boldsymbol{R}$ and the camera position $\lambda \underline{t}$ with an unknown scale factor λ. With the reference length L defined by two points $\underline{X}$ and $\underline{Y}$ of the calibration object, the scale factor λ can be determined via a non-linear optimization method (e.g. the Marquardt-Levenberg method) where the criterion to fulfill is $\left| \underline{X}(\lambda) - \underline{Y}(\lambda) \right| = L$.

The above-described method assumes that the global coordinate system is identical to the coordinate system of the second camera. However, after the calibration procedure, the global coordinate system can be translated and rotated to any desired position, e.g. in order to align the global coordinate system with the aerodynamic model. This is achieved by four reference point markers indicating the new coordinate system position and orientation.

3.3 Calibration Objects and Calibration Procedure

A planar target with a point structure is used for the photogrammetric camera calibration. This is accomplished with a black anodized aluminum plate with holes of 0.01 mm depth drilled into the surface to create well-defined calibration markers. During the calibration procedure, the plate is translated by defined distances in order to generate a three-dimensional set of calibration points. For the self-calibration, a two-point target is used, which consists of a low-distortion carbon-fiber rod with two point-source LEDs mounted at the tips. A control unit is attached in order to flash the LEDs synchronously with the frame rate of the cameras (Fig. 2). Such a "virtual" target can be produced at low cost, with a high accuracy at any size and is very simple to manipulate. An

---

[1] Here *normalized* is understood as image coordinates of a perfect camera with f=1 (Hartley and Zisserman, 2000).
[2] The point distribution mean is located at (0,0) and the standart deviation is $\sqrt{2}$. For the motivation of this normalization see Hartley, 1997.

LED aperture of 60 µm, a light emission angle of 100 degrees and a flash duration of 270 µs ensure sharp point images suitable as calibration markers. For the generation of the calibration data the stick is moved randomly in the entire measurement volume. This gives a sequence of image pairs, each of which corresponds to the image of the calibration stick at one position. Since only two points exist in any given image, the assignment of corresponding points is straightforward. Figure 3 shows an example of the overlay of 600 image pairs.
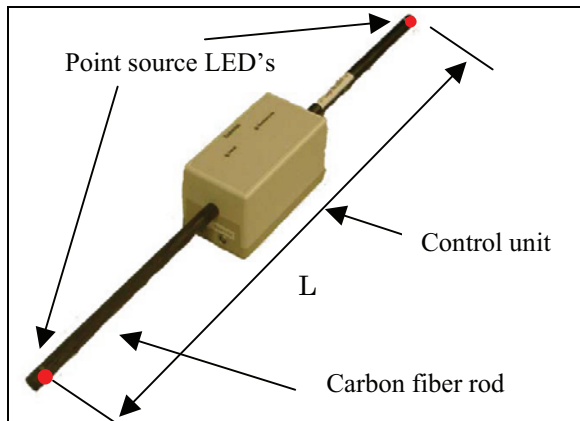
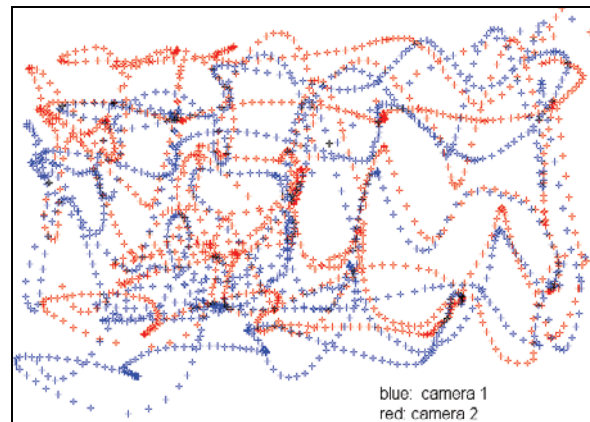Fig. 2. Mobile calibration target featuring two point source LEDs mounted at the tips of a rod.

Fig. 3. Overlay of 600 image pairs produced by the calibration rod.

4. Two-dimensional Path Reconstruction

The extracted path line boundary cannot be directly used for the three-dimensional reconstruction of the path lines and a representation of a path line in the different camera views is needed. The bubble tracks of finite thickness must be reduced to a representative line close to the centerline of the path line. The direct use of a skeleton algorithm proved insufficient, because of the sensitivity to noise, the slow execution time and the limitations on achievable pixel accuracy. As an alternative, an approximating parametric spline model based on B-splines (Dierckx, 1993) can be used to represent the path lines.

Splines have several desirable properties (e.g. smoothness, continuity, built-in boundedness, decoupling of the x and y coordinates, local controllability and a low-order data representation of a curve) and can accurately describe lines with a complex shape. For the present case, B-splines of third degree and fixed knots are chosen.

A crucial aspect in the processing chain is the configuration of the digital cameras which record the bubble images. The bubbles are illuminated with a continuous light source and are recorded with the maximum exposure time (=1/frame rate) by an interline CCD chip with a negligible read-out time. This results in a set of consecutive images, in which a moving particle produces a continuous string of connected path segments, which form a path line (Figs. 1 and 4). Previous attempts (Machacek and Rösgen, 2001) have shown that path line reconstruction based on the analysis of independent path line segments (i.e., independent image frames) can lead to topologically inaccurate solutions due to the difficulty involved in processing the segment end points in a consistent manner when the information of the previous and following segments is not taken into account. Hence in the present approach the processing is based on multi-frame path lines as reconstructed from a connected set of path line segments.

The initial low-level processing is achieved with the following steps: background subtraction, binarization with an appropriate thresholding operator and median filtering to reduce the residual noise. The current image is then scanned in the immediate vicinity of the path line segment endpoints detected in the previous frame (Fig. 4a). In case of a successful match, the new segment boundary and its two endpoints are extracted based on a boundary curvature criterion. This procedure is continued until a path line is completed (i.e., until the particle disappears from the camera field of view, Fig. 4c). Thereafter, the representation in spline form of the path line can be calculated, whereby the main difficulty lies in the fact that no points of the approximate spline are known. The path line boundary pixels are taken to find a first estimate. Based on the extracted endpoints (two for each segment), the segment boundary pixels are sorted and associated with a parameter ascending from the first endpoint up to the second endpoint. The parameter increments between adjacent boundary pixels are chosen to be equidistant. For a path line of moderate shape complexity, the initial spline will already be a good approximation, as can be seen in Fig. 4c. A new, ordered set of data points is defined as the center of the two intersection points between a line perpendicular to the current spline curve and the boundaries of the path line (Fig. 4c). A new spline approximation is then calculated based on these data points. In most cases, one iteration is sufficient to generate a spline that represents the particle path line well (Fig. 4d).

If two (or more) path segments cross each other in the same frame, the difficulty involved in segment separation increases. The present method does not take crossing path lines into consideration. Therefore, the two-dimensional reconstruction will fail for measurements in flows with high seeding densities, where many crossing path segments in a frame are to be expected.
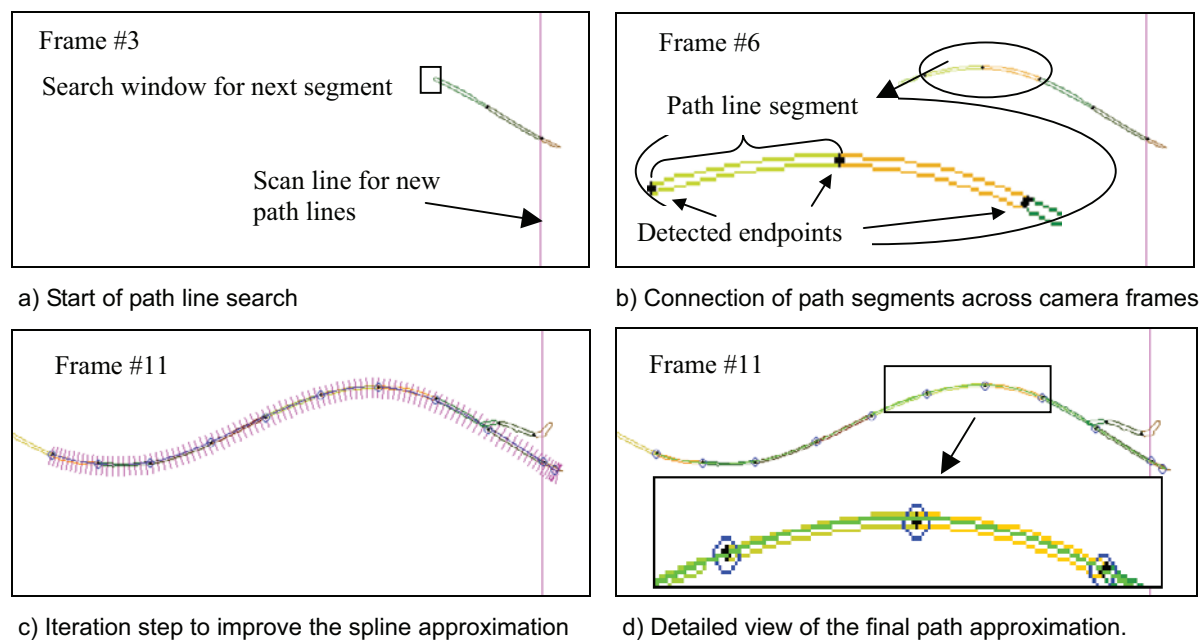

Fig. 4. Processing steps for a multi-frame path line.

5. Three-dimensional Path Reconstruction

For the calculation of the path line coordinates in three-dimensional space, corresponding point pairs on corresponding path lines have to be found in both camera views. As a first step, corresponding path lines are found based on corresponding end points as follows: the end points of a

path line segment are projected into the second camera image, creating epipolar lines (red lines in Fig. 5). If the distance between the epipolar line projection and an endpoint is below a critical value, the endpoints and thus the path lines are considered to correspond. Since the epipolar condition for points in a two-camera configuration is ambiguous, all path line end points are tested for correspondence so as to create a unique solution.
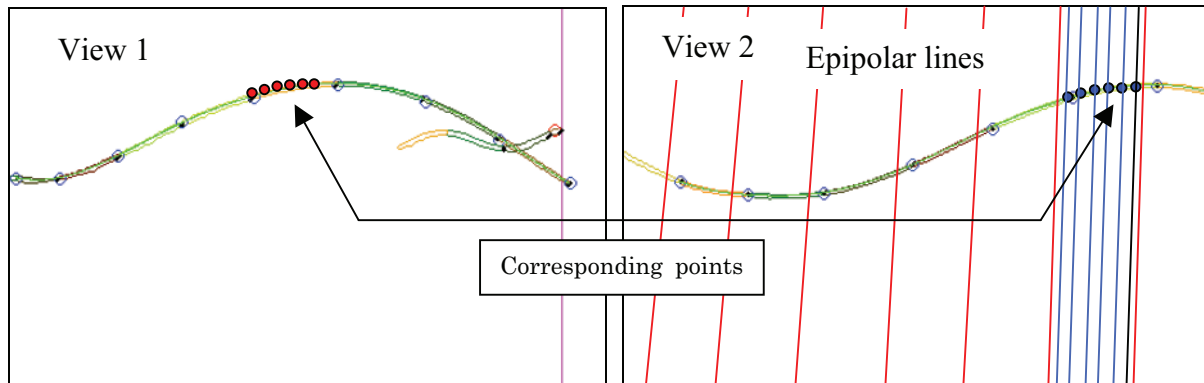

Fig. 5. Relationship between view 1 and view 2 as given by the epipolar lines.

After corresponding path splines are found, corresponding points have to be determined. Two possible methods of correspondence point building were tested. The first method is photogrammetrically consistent in the sense that the point pairs truly correspond. This is achieved by projecting image points from a path line in view 1 into view 2, which yields a set of epipolar lines (blue lines in Fig. 5). These lines are intersected by the corresponding path spline in view 2, thus creating the corresponding points. In the second method, points are defined independently at equidistant intervals on the same segment in both views. Because length ratios are not invariant for a projective mapping, these points do not truly correspond. However, because the path line segments have a finite extent in space, the introduced error is finite and for the present set-up, the projection error is estimated to be less than 0.5 pixels. A test has shown that the photogrammetrically consistent reconstruction does not differ significantly from the approximation. For cases where the intersection angle between the spline and the epipolar line is small, the intersection point calculation is likely to be sensitive to errors. In contrast, the approximate method is much simpler and more robust, and hence is the preferred choice. The number of points per segment used for the 3D reconstruction is chosen based on the segment length and complexity. All corresponding 2D point pairs are used to calculate the coordinate points in three-dimensional space, and the path line is thus reconstructed as a sequence of points. Finally, these three-dimensional points are used to rebuild a three-dimensional spline representation of degree three, fixed knots of the path line. This spline curve is also based on third-order B-splines.

After the spline representations of the path lines are calculated in three-dimensional space, the topological features of the individual path lines are analyzed. The topology of a three-dimensional curve can be characterized by the tangent vector the normal vector and the binormal vector (the Frenet frame). Associated with this set of vectors are the arc length, the curvature and the torsion defined by the Serret-Frenet formulas. The arc length is integrated numerically with the Gauss-Legendre algorithm (with a Legendre polynomial of degree 10), and the Frenet frame is calculated analytically with the derivatives calculated from the spline coefficients according to the formula given by Dierckx, 1993. The arc length of a path line segment gives a direct estimation of the average velocity along the path line segment, and the curvature and torsion are local criteria for the classification of the individual path lines.

6. Results

6.1 Camera Calibration

The two-step camera calibration was compared with a full photogrammetric calibration for a given camera set-up. The comparison showed that by increasing the number of matching point pairs for the self-calibration part, the external camera parameters converged well toward the photogrammetric solution. The difference in the camera orientation was less than $2*10^{-3}$ degrees, and the difference in the camera position was less than 2.5 mm. The distance between the epipolar line and the corresponding point is a direct indicator of the quality of the essential matrix. For a typical calibration in the wind tunnel with 500 images (corresponding to 1000 matching points), an averaged epipolar line–point distance of 0.1 pixels units (= 0.00011 normalized units) was achieved. The metric accuracy of the two-step calibration can be given based on the estimated calibration bar length L. A typical calibration, again with 500 images, shows a calibration length estimation with a standard deviation of 0.7 mm or a relative standard deviation of 0.14% (based on L). If a segment length of 10 cm is assumed, a theoretical velocity accuracy of $6*10^{-5}$ m/s would be achieved.

6.2 Demonstration Measurements

The proposed quantitative visualization method was demonstrated in a medium-scale wind tunnel facility (see section 2) for a free-stream flow, a stagnation point flow around a circular flat plate with a diameter of 0.7 m and for the vortex system formed behind a delta wing (wing span 80 cm). The free-flow measurement was used to estimate the accuracy of the velocity measurement. The stagnation point flow experiment was used to measure a well known and relatively simple configuration. Finally, the delta wing measurement was used to demonstrate the applicability of the system to complex three-dimensional flows. The measurements consist of an average of 2500 image pairs (measurement time: 20.8 s). No filtering is performed on the obtained path lines. The path line color indicates the flow velocity, where red corresponds to high velocity and blue corresponds to low velocity. Figure 6 shows the visualization of the free-stream flow experiment. For an evaluation, the velocities were averaged in 0.2-m-wide segments perpendicular to the mean flow direction (Test 1 and Test 2 in Fig. 7) and were compared with complementary measurements via a propeller anemometer (Ref1, Ref2, Ref3). The velocities measured with the present method are for the most part within of the error tolerance band of the propeller anemometer measurements, but the present method predicts a stronger velocity gradient. The visualization of the stagnation point flow around
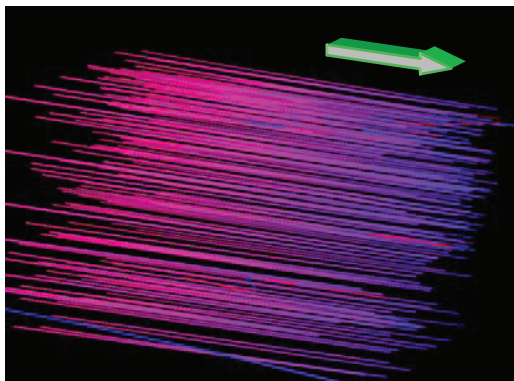

Fig. 6. Free stream flow experiment (Test 2) in the wind tunnel (188 path lines with 2197 segments). Measurment time was 22 seconds.
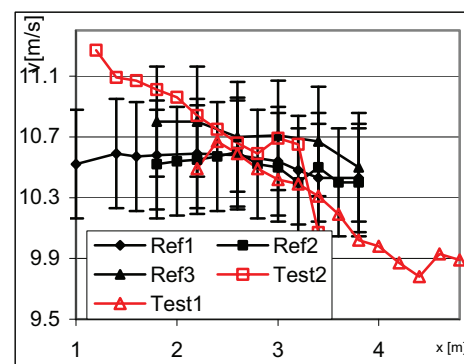

Fig. 7. Averaged velocity from the free-stream flow experiments compared with propeller anenometry measurements.

a circular plate is shown in Figs. 8. and 9. The inflow velocity was 8.5 m/s. The path lines indicate clearly the region of the stagnation point and the deceleration and acceleration of the flow around the plate. However, it can also be seen that no data close to the plate and very little data on the flow behind the plate is available. In fact, this shows one of the main difficulties of the method; to arrange the lighting such that an optimal illumination of the test section is achieved. The results for the delta wing experiment are shown in Figs. 10, 11 and 12. These demonstrate that the method is applicable to the measurement of complex three-dimensional flows. However, for the reason mentioned in the circular plate experiment, little data is available near the top surface of the delta wing. In addition, as a result of low seeding density, little data is available near the vortex core. Finding the optimal seeding density also proved to be difficult since too high a particle density results in conditions that make the image processing difficult (i.e. crossing segments). Yet, the current results do not represent the limits of the proposed method and improved results can be expected for improved illumination and seeding settings.
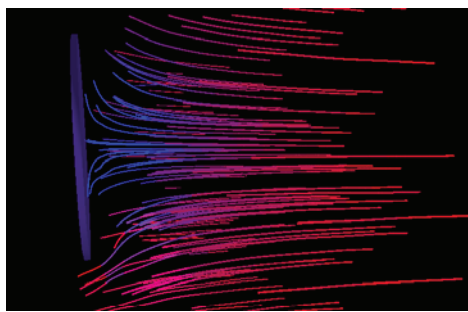

Fig. 8. Path lines of a flow around a circular flat plate (133 path lines with 909 segments).
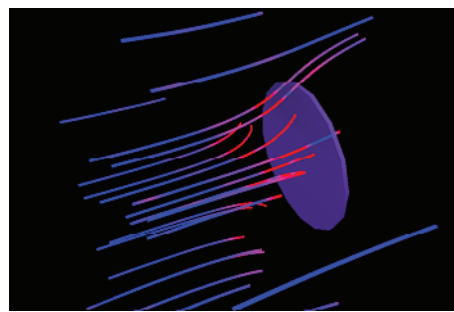

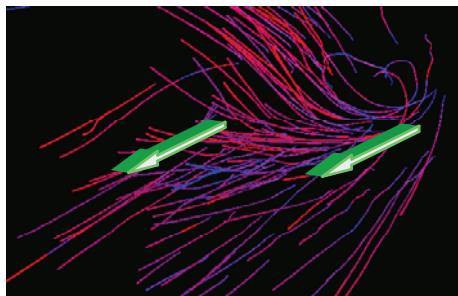Fig. 9. Color indicates the curvature (24 path lines with 174 segments).

Fig. 10. Vortex formation behind a delta wind, as viewed from behind. The arrows indicate the flow direction.
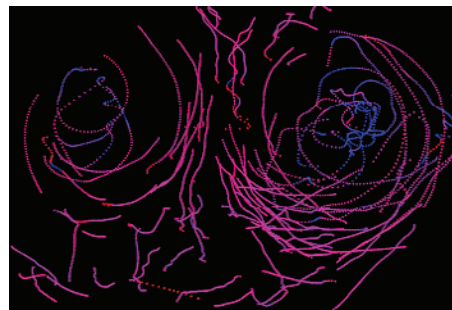

Fig. 11. Projection of the path lines from Fig. 10 onto a virtual plane perpendicular to the mean flow direction.
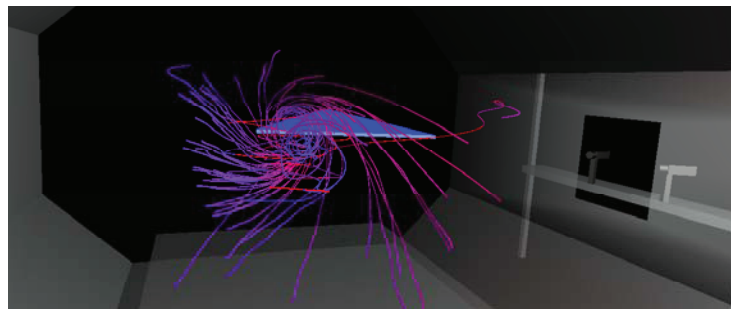

Fig. 12. Vortex formed behind a delta wing in the interactive virtual wind tunnel environment. The observation window and the two cameras are visible on the left.

7. Conclusions

The method presented herein yields true 3D flow measurements and visualizations, where the depth of the measurement volume is of the same order as the length (resp. width). The results give insight into the flow topology with additional quantitative information. By approximating splines based on third-order B-splines, the medial line of a composite, multi-frame path line can be accurately captured. The two-step camera calibration gives accurate estimates of the camera parameters and is simple and can be performed quickly in large measurement volumes. The final 3D path lines are also represented with a model based on third-order B-splines. These analytical curves provide accurate and continuous representations of the path lines and form a base from which topological information about the flow can be extracted. Compared to three-dimensional particle tracking (3D-PTV), the present method does not require elaborate tracking algorithms and provides continuous information on the particle path. The achievable seeding density, which is a crucial factor in spatial measurement data density, is clearly lower compared to that of classical 3D-PTV methods. This is due to the fact that the crossing of particle path segments is much more likely to occur than the overlapping of discrete particle locations. In the demonstration experiments performed herein, the average number of particles in one frame was 5. However, this is not the maximum achievable particle seeding density for the present method, and upon implementation of an algorithm to handle crossing segments, the seeding density can be increased further. Nevertheless, the spatial measurement data density for the present measurements is high enough to enable a comprehensive quantitative visualization, such as that shown in Figs. 6 and 8-12.

Acknowledgements

References

Borghese, N. A. and Cerveri P., Calibrating a Video Camera Pair with a Rigid Bar, Pattern Recognition, 33 (2000).

Doh, D. H., Kim, D. H., Cho, K. R., Cho, Y. B., Lee, W. J., Saga, T. and Kobayashi, T., Development of Genetic Algorithm Based 3D-PTV Technique, Journal of Visualization, 5-3 (2002), 243-254.

Dierckx, P., Monographs on Numerical Analysis: Curve and Surface Fitting with Splines, Oxford Science Publications, (1993).

Hartley, R. I., In Defense of the Eight-Point Algorithm, IEEE Transactions on Pattern Analysis and Machine Intelligence, 19-6 (1997).

Longuet-Higgins, H. C., A Computer Algorithm for Reconstructing a Scene from Two Projections, Nature, 293 (1981), 133-135.

Machacek, M. and Rösgen, T., Development of a Quantitative Real-Time Visualization Tool Based on 3D-PTV, Proc. 9th Int. Symp. on Flow Visualization, Edinburgh, (2000), 199.1-199.9

Machacek, M. and Rösgen, T., Development of a Quantitative Flow Visualization Tool for Applications in Industrial Wind Tunnels, Proceedings of the 19th Int. Congress on Instrumentation in Aerospace Simulation Facilities, Cleveland, Ohio, (2001).

Hartley, R. and Zisserman, A., Multiple View Geometry in Computer Vision, Cambridge University Press, (2000).

Takehara, K. and Etoh, T., A Study on Particle Identification in PTV-Particle Mask Correlation Method-, Journal of Visualization, 1-3 (1999), 313-323.

Author Profile

Thomas Rösgen: He is a Professor of Fluid Dynamics at the Institute of Fluid Dynamics/ETH Zurich. Following his Ph.D. studies in aeronautics at the California Institute of Technology (Pasadena, USA) he held several positions at Stuttgart University (Germany) and the Technology Research Center of the European Space Agency (ESA-ESTEC, Noordwijk, Netherlands). His research activities are primarily in the area of modern electro-optical and imaging diagnostics for fluid dynamical applications.

Matthias Machacek: He studied mechanical engineering at ETH Zurich and presented his master's thesis in 1998 based on research conducted at the Turbulence and Heat Transfer Laboratory of the University of Tokyo, where he was a visiting researcher in 2000. He is curently where he received his Ph.D. degree in 2003 at the Institute of Fluid Dynamics/ETH Zurich.